

10/02/2016

KIC 8262223: A Post-Mass Transfer Eclipsing Binary Consisting of a Delta Scuti Pulsator and a Helium White Dwarf Precursor

Zhao Guo, Douglas R. Gies, Rachel A. Matson

*Center for High Angular Resolution Astronomy and Department of Physics and Astronomy,
Georgia State University, P. O. Box 5060, Atlanta, GA 30302-5060, USA;
guo@chara.gsu.edu, gies@chara.gsu.edu, rmatson@chara.gsu.edu,*

Antonio García Hernández

*Instituto de Astrofísica e Ciências do Espaço, Universidade do Porto, CAUP, Rua das
Estrelas, PT4150-762 Porto, Portugal;
agh@astro.up.pt*

Zhanwen Han, Xuefei Chen

*Key Laboratory for the Structure and Evolution of Celestial Objects, Yunnan Observatories,
the Chinese Academy of Sciences, Kunming, 650011, P.R. China
cxf@ynao.ac.cn, zhanwenhan@ynao.ac.cn*

ABSTRACT

KIC 8262223 is an eclipsing binary with a short orbital period ($P = 1.61$ d). The *Kepler* light curves are of Algol-type and display deep and partial eclipses, ellipsoidal variations, and pulsations of δ Scuti type. We analyzed the *Kepler* photometric data, complemented by phase-resolved spectra from the R-C Spectrograph on the 4-meter Mayall telescope at Kitt Peak National Observatory and determined the fundamental parameters of this system. The low mass and oversized secondary ($M_2 = 0.20M_\odot$, $R_2 = 1.31R_\odot$) is the remnant of the donor star that transferred most of its mass to the gainer, and now the primary star. The current primary star is thus not a normal δ Scuti star but the result of mass accretion from a lower mass progenitor. We discuss the possible evolutionary history and demonstrate with the MESA evolution code that the system can be understood as the result of non-conservative binary evolution similar to that for the formation of EL CVn type binaries. The pulsations of the primary star can be explained as radial and non-radial pressure modes. The equilibrium models

from single star evolutionary tracks can match the observed mass and radius ($M_1 = 1.94M_\odot$, $R_1 = 1.67R_\odot$) but the predicted unstable modes associated with these models differ somewhat from those observed. This work presents a preliminary asteroseismic analysis of the abnormal δ Scuti pulsators, and we discuss the need for better theoretical understanding of such pulsating mass gaining stars.

1. Introduction

The δ Scuti variables are A- or F-type main-sequence (MS) and post-MS stars. They are interesting asteroseismic targets as they are numerous and often show multi-periodic pressure mode pulsations. However, it is hard to determine their fundamental parameters, and their ubiquitous fast rotation makes this task even more difficult. Those eclipsing binaries (EBs) with a component that is a δ Scuti pulsator offer us the means to determine accurate masses and radii for these variables. However, systems with short orbital periods are more likely to be observed and these are also more likely to experience binary interactions. Many δ Scuti pulsating stars in Algol-type (oEA) systems were discovered from ground-based photometry (Mkrtychian 2002, 2003; Soydukan et al. 2006). The daily gaps in the time series limit the number of detected pulsation frequencies to only a few. Space missions like *Kepler* and *CoRoT* have provided continuous and accurate light curves of hundreds of δ Scuti pulsating EBs and tens of frequencies have been detected. Most of the systems that have been studied in detail were considered as single stars and understood from the theory of single star evolution (Hambleton et al. 2013; Maceroni et al. 2014; da Silva et al. 2014). In this paper, we focus on δ Scuti EBs which have undergone binary interactions. KIC 10661783 (Southworth et al. 2011; Lehmann et al. 2013) belongs to this class, and this binary consists of an oversized low mass secondary ($M = 0.2M_\odot$, $R = 1.13R_\odot$) and a δ Scuti pulsating primary.

KIC 8262223 ($K_p = 12.146$, $\alpha_{2000}=20:01:19.788$, $\delta_{2000}=+44:08:38.90$) is included in the Kepler Eclipsing Binary Catalog (Prša et al. 2011; Slawson et al. 2011). It is described as a semi-detached eclipsing binary with an orbital period of 1.612 days, a near circular orbit, and a high inclination ($\sin i = 0.97$). The eclipse timing analysis of this system was performed by Gies et al. (2012, 2015) and Conroy et al. (2014). The flat $O - C$ diagram of the timings indicates that this circular binary is not likely to have a nearby third companion. Gies et al. (2012) also noticed a pulsation signal in near resonance with the orbit in the light curve. Armstrong et al. (2014) estimated the effective temperatures of the primary and secondary as $T_{\text{eff1}} = 9325 \pm 428$ K and $T_{\text{eff2}} = 6791 \pm 642$ K, respectively, based on their fit of the binary spectral energy distribution (SED).

2. *Kepler* Photometry and Ground-based Spectroscopy

Simple Aperture Photometry (SAP) data (Data Release 23) from the *Kepler* satellite were retrieved from the MAST Archive. There are 18 quarters (Q0-17) of long cadence data and 1 quarter (Q4) of short cadence data. The aperture contamination is lower than 0.7% in all quarters except for Q12 (1.3%). The light curve shows deep eclipses, ellipsoidal variations and coherent pulsations at frequency about 65 d^{-1} as apparent in the short cadence data. A sample of the short cadence light curve is shown in Figure 1. As the main pulsational frequency is well above the Nyquist frequency ($\approx 24 \text{ d}^{-1}$) of long cadence data (30 minutes sampling), these pulsations are essentially all cancelled out in the long cadence measurements. Thus we used the long cadence data for binary light curve modeling and the light curve residuals of short cadence data for pulsational analysis.

We also obtained 13 ground-based spectra of moderate resolving power ($R \approx 6000$) from the R-C Spectrograph on Kitt Peak National Observatory (KPNO) 4-meter Mayall telescope from 2010 to 2013. The spectra cover the wavelength from 3930 \AA to 4600 \AA , with typical signal-to-noise ratio of $70 - 120$ (Figure 2). More information about the instrument and spectra can be found in Matson et al. (2016).

3. Spectroscopic Orbit and Atmospheric Parameters

The radial velocities (RVs) were determined following the same cross-correlation technique described by Matson et al. (2016). Two templates from atmospheric model grids UVBLUE (Rodríguez-Merino et al. 2005) were cross-correlated with the observed spectra to obtain the radial velocities presented in Table 1. The derived RVs were fitted to get the orbital parameters ($K_1, K_2, \gamma_1, \gamma_2, T_0$) with the Levenberg-Marquardt algorithm, where K_1, K_2 and γ_1, γ_2 are semi-amplitude velocities and system velocities of the primary and secondary star, respectively; T_0 is time epoch of the primary minimum (Figure 3). We searched for a circular orbital solution ($e = 0$) and the orbital period was fixed to the value from eclipse timing measurements in Gies et al. (2015) as $P = 1.61301476$ days. We then used the tomography algorithm (Bagnuolo et al. 1994) to reconstruct the individual component spectra of two stars. These spectra were compared with a grid of UVBLUE synthetic spectra and the best atmospheric parameters ($T_{\text{eff}}, \log g, [\text{Fe}/\text{H}]$ and $v \sin i$) were determined from a grid search followed by a local optimization with the Levenberg-Marquardt algorithm. To break the degeneracy in fitting five atmospheric parameters, the $v \sin i$ values were initially estimated from the metal lines in five different spectral sections and the $\log g$ values were fixed to the result from the binary modeling (see next section). Note that the uncertainties were estimated from the covariance matrices, and these can be somewhat underestimated.

The procedures mentioned above are iterative, and in each step the templates and RVs were updated from previous determinations. We adopted the final values when the parameters converge.

Spectral disentangling is another way of deriving orbital parameters. For spectroscopic binaries, we observe the linear combination of two component spectra with different Doppler shifts. Given the radial velocities of the two stars and their mean flux ratio, we can form a coefficient matrix A . Then we can separate the component spectra by solving the linear inverse problem $y = Ax$, where y and x are vectors formed by concatenating the observed composite spectra and the individual component spectra (see Hensberge et al. 2008). If the RVs used in the coefficient matrix are calculated from orbital parameters, we can find the optimized orbital parameters by minimizing the χ^2 differences between the observed and synthetic composite spectra, $|y - AX|^2$. We implemented this method with the FDBinary code (Ilijic et al. 2004). Note that the code uses a downhill simplex optimizer and regrettably does not provide uncertainty estimates.

The final orbital parameters are summarized in Table 2. The orbital parameters from the two techniques agree very well (Figure 3). The results show that the system has a very small mass ratio ($q = 0.104$), and the systemic velocities from fitting RVs of primary and secondary (γ_1, γ_2) agree within uncertainties. Table 3 contains the optimal atmospheric parameters. This binary consists of a hot A-type primary ($T_{\text{eff1}} = 9128$ K) and a much cooler secondary ($T_{\text{eff2}} = 7119$ K). Both stars have metallicities slightly lower than solar. The projected rotational velocity of the primary star ($v \sin i = 37 \pm 13$ km s $^{-1}$) is a little lower than the synchronized value at 50 km s $^{-1}$ (see Table 4 in next section). The $v \sin i$ of the secondary matches the synchronized value very well. Note that each pixel in our spectra is equal to 26.25 km s $^{-1}$ in velocity space, and we cannot reliably measure small rotational velocities ($v \sin i < 30$ km s $^{-1}$). In Figure 4, we show the reconstructed component spectra of the two stars and the best matching model spectra. The mean flux ratio (F_2/F_1) in the observed spectral range (≈ 4225 Å) is 0.21 ± 0.02 which amounts to percentage contributions of 82.6% and 17.4% for the primary and secondary, respectively.

4. ELC Binary Models

We used the *Kepler* long cadence data to perform our light curve modeling. The preparation of the raw data, which was detailed in Guo et al. (2016), includes de-trending and outlier removal. We divided the 18 quarters into eight sections ($Q0 - Q2$, $Q3 - 4$, $Q5 - 6$, $Q7 - 8$, $Q9 - 10$, $Q11 - 12$, $Q13 - 14$, $Q15 - 17$) and fitted the light curve of each individually. The standard deviations of the best fitting parameters from these eight datasets are adopted

as the final uncertainties.

We used the Eclipsing Light Curve (ELC) code by Jerome Orosz (Orosz & Hauschildt 2000) to model the binary light curve. The code implements the Roche model and synthesizes the binary light curve and radial velocity curve by integrating the specific intensity and flux-weighted RVs of each segment on the stellar surface.

We optimized the following fitting parameters: orbital inclination (i), temperature ratio ($temprat = T_{\text{eff2}}/T_{\text{eff1}}$), filling factors (f_1, f_2) and time of secondary minimum (T_0) by implementing the genetic algorithm PIKAIA (Charbonneau 1995). We set broad search ranges for these parameters: $i \in [50, 90]$ (degrees), $temprat \in [0.6, 0.9]$, $f_1, f_2 \in [0.1, 0.8]$, $T_0 \in [55430.9, 55432.5]$ (HJD-2,400,000). The orbital period was fixed to 1.61301476 days as found by Gies et al. (2015). The effective temperature of the primary was fixed to the value from spectroscopy (9128 K) as it is well known that the light curve is only sensitive to the temperature ratio. We assumed the binary has a circular orbit and the two components have synchronized rotation as indicated from spectroscopy. The parameters mass ratio ($q = M_2/M_1$), velocity semi-amplitude (K_1), and systemic velocity (γ) were fixed to values from spectroscopic orbital solutions as they have little affect on the light curve. The gravity brightening coefficients (β) were fixed to the canonical values of 0.25 for radiative atmospheres and 0.08 for convective atmospheres. Similarly, the surface bolometric albedos (l_1, l_2) were set to 1.0 and 0.5 for radiative and convective atmospheres, respectively. However, the light curve residuals from the parameter settings above still show obvious variations. We found that by setting l_2 as a free parameter the light curve fit is much better. The optimal value of l_2 is 0.22, which is much lower than the canonical value of 0.5. Note Matson et al. (2016) also found a lower albedo (0.33) for the F stars in KIC 5738698. If we let the albedo of the primary star (l_1) vary, the best value is very close to 1.0, and the light curve fit is not improved.

Doppler boosting or beaming is a relativistic effect, in which the observer will receive a higher photon rate from a star moving towards him or her, and vice versa. The fractional change of photon rate is $\Delta n_\lambda/n_\lambda = f_{\text{DB}} v_\lambda/c$, where v_λ is radial velocity of the star and c is speed of light. Thus, the key parameters are the mass and flux ratios. If the two stars have similar temperature, then the beaming effect will be canceled out if they have a mass ratio of 1. For systems with a very small mass ratio, the Doppler beaming effect is expected to play an important role. A measurement of the beaming amplitude from the light curve can provide an independent estimation of the orbital parameters. This was performed in many beaming binaries such as KOI-74, KOI-81 (van Kerkwijk et al. 2010) and KIC 11558725 (Telting et al. 2012). In the ELC code, the Doppler beaming effect is accounted for following the treatment in van Kerkwijk et al. (2010). The beaming parameter f_{DB} is estimated as

the wavelength average of $xe^x/(e^x - 1)$ in the *Kepler* passband, where $x = hc/(\lambda kT)$. The estimated values are 2.76 and 3.48 for the primary and secondary, respectively, and are fixed in the fitting process. In Figure 5, we show the best light curve solution and corresponding residuals with (red) and without (green) Doppler beaming. It can be seen in the two middle panels that the residuals are more symmetric around the zero horizontal line if the beaming effect is included. We also show the ELC model of the Doppler beaming signal in the bottom panel, and the amplitude of the beaming effect is about 0.00033 magnitude. It is interesting to note that the photometric analogue of the spectroscopic Rossiter-McLaughlin effect can be seen at phases 0.0 (Groot 2012).

In Table 4, we list the final model parameters of KIC 8262223. The parameters of the primary are typical for a mid-A type ZAMS star ($M_1 = 1.94M_\odot$, $R_1 = 1.67R_\odot$, $T_{\text{eff1}} = 9128$ K) but somewhat over-luminous. The secondary has a very low mass ($M_2 = 0.20M_\odot$) and very discrepant radius ($R_2 = 1.31R_\odot$) and effective temperature ($T_{\text{eff2}} = 6849$ K) compared to main sequence stars of the same mass. This suggests that this system has gone through binary evolution with mass transfer. The implications and possible evolutionary scenarios are discussed in section 6.

The optimal effective temperature ratio ($T_{\text{eff2}}/T_{\text{eff1}}$) from fitting the light curve is 0.75, and this gives $T_{\text{eff2}} = 6849$ K which is 270 K (1.8σ) cooler than that from spectroscopy ($T_{\text{eff2}} = 7119$ K). This discrepancy can be explained by our adopted lower albedo $l_2 = 0.22$. There is a correlation between T_{eff2} and bolometric albedo l_2 . If we fixed l_2 to the canonical value of 0.5 – 0.6, then the optimal $T_{\text{eff2}}/T_{\text{eff1}}$ value is much higher (0.78), which agrees well with the spectroscopic result. As we cannot get a very good light curve fit with l_2 fixed to 0.5, we seem to have a dilemma. It is known that the bolometric albedo is difficult to pin point and is usually treated as a free parameter. Sometimes even values as high as 2.46 are used (e.g., star A in KIC 10661783; Lehmann et al. 2013). Note that the effective temperature of KIC 3858884 star B from spectroscopy by Maceroni et al. (2014) is also ≈ 300 K different from that from the light curve solution. Thus, we think this minor discrepancy is not an unexpected problem for our analysis.

5. Pulsational Characteristics

Only the short cadence data can be used to study the pulsations of this system. We calculated the Fourier spectrum of the light curve residuals with the *Period 04* package (Lenz & Breger 2005) with all eclipses truncated. The calculation was performed to the short cadence Nyquist frequency ($\approx 734 \text{ d}^{-1}$) with the fitting formula $Z + \sum_i A_i \sin(2\pi\Omega_i t + 2\pi\Phi_i)$, where Z, A_i, Ω_i, Φ_i are the zero-point shift, pulsation amplitudes, linear frequencies

and phases, respectively, and time $t = \text{BJD} - 2,400,000$. No significant peaks were found beyond 70 d^{-1} . All frequencies with $S/N > 4$ are reported in Table 5 and the Fourier spectrum is shown in Figure 6. The uncertainties were calculated following Kallinger et al. (2008).

Almost all the pulsations are in the range of $50 - 65 \text{ d}^{-1}$. There appear to be some low amplitude peaks at $100 - 130 \text{ d}^{-1}$ (not shown in Figure 6) which are exactly twice the main pulsation range. We interpret these peaks as the harmonics of the main pulsations rather than some high intrinsic pulsation frequencies. This indicates that the pulsations are to some extent non-sinusoidal. The primary star contributes much more light (83% in the wavelength range of our spectra), and its fundamental parameters ($M_1 = 1.94M_\odot$, $R_1 = 1.67R_\odot$, $T_{\text{eff}1} = 9128 \text{ K}$) also agree with those of a typical δ Scuti pulsator. It is, thus, very likely that the pulsations stem from the primary. The pulsations at $50 - 65 \text{ d}^{-1}$ can be well explained as high order ($n_p \approx 6, 7$) radial and non-radial p-modes.

In the low frequency region, there are two peaks $f_{20} = 1.2397 \text{ d}^{-1}$ and $f_{58} = 0.79928 \text{ d}^{-1}$. f_{20} is equal to twice of orbital frequency $2f_{\text{orb}} = 2 \times 0.61996 \text{ d}^{-1}$ within uncertainties and is likely the result of imperfect light curve fitting (e.g., ellipsoidal variations). f_{58} is probably due to a low-frequency g-mode.

As the star is pulsating at relatively high radial orders, which are closer to the asymptotic regime, we can expect to find some frequency regularities similar to those observed in solar-like oscillators. García Hernández et al. (2015) found the signature of frequency regularities in six δ Scuti stars in eclipsing binaries by analyzing the Fourier Transform (FT) of the p-mode frequencies. These frequency patterns are close to the large frequency separation which is related to the mean stellar density. We applied the same FT technique to the frequencies in Table 5, and the Fourier spectrum is presented in Figure 7. The periodicity at $39.9 \mu\text{HZ} = 0.5\Delta\nu_{\text{obs}}$ is related to the large frequency separation. From the mean density of the primary, we can deduce the expected large separation ($\Delta\nu$) by using the linear relation between $\log \Delta\nu$ and $\log \rho$ (Suárez et al. 2014; García Hernández et al. 2015). The expected $\Delta\nu$ is $70.7 \mu\text{HZ}$, which is similar to but smaller than the observed value $\Delta\nu_{\text{obs}} = 2 \times 39.9 = 79.8 \mu\text{HZ}$. Paparo et al. (2016a, b) found the signatures of the large frequency separation in 90 δ Scuti stars observed by *CoRoT* satellite, and except for showing regularities of $\Delta\nu$, some of them show patterns which approximately agree with $\Delta\nu \pm f_{\text{rot}}$ or $\Delta\nu \pm 2f_{\text{rot}}$. If we adopt the synchronous rotational frequency $f_{\text{rot}} = 7.175 \mu\text{HZ}$, the corresponding rotational splittings for the high order p-modes are $m(1 - C_{nl})f_{\text{rot}} \approx mf_{\text{rot}}$ (Aerts et al. 2010), and $m = \pm 1$ and $m = \pm 1, \pm 2$ for $l = 1$ and $l = 2$ modes, respectively. We thus conclude that the observed pattern $\Delta\nu_{\text{obs}}$ agrees with the theoretical large frequency separation with rotational effect taken into account. Indeed, the highest peak in the Fourier spectrum in Figure 7 is at

about $7.07\mu\text{HZ}$ which is only slightly smaller than the orbital frequency $f_{\text{orb}} = 7.175\mu\text{HZ}$, and thus this regularity is likely the result of rotational splitting.

To check whether the pulsation range can be explained by the non-adiabatic theory, we modeled the evolution of some single non-rotating stellar models with MESA (Paxton et al. 2011, 2013) and calculated their pulsation frequencies in the range of $20 - 70 \text{ d}^{-1}$ with GYRE (Townsend & Teitler 2013). We set the mixing length parameter α_{MLT} to 1.8 and used the OPAL opacity tables (Iglesias & Rogers 1996). Solar mixtures in Grevesse & Sauval (1998) were adopted for the assumed solar composition. The results are presented in Figure 8. The pulsation modes ($l = 0, 1, 2$) from the equilibrium model with $M = 1.94M_{\odot}$, $R = 1.67M_{\odot}$, $Y = 0.28$, and $Z = 0.02$ are all stable ($\eta < 0$). However, we note that the peak of the stability parameter η (the normalized growth-rate defined in Stellingwerf 1978) is at $60 - 65 \text{ d}^{-1}$ which roughly agrees with the observed unstable range $50 - 65 \text{ d}^{-1}$. Note that modes from a similar but slightly less massive model with $M = 1.79M_{\odot}$, $R = 1.67R_{\odot}$, $Y = 0.28$, and $Z = 0.02$ can produce unstable p-modes (positive η) in the range of $55 - 60 \text{ d}^{-1}$. We have to be cautious in interpreting the above analysis based on single star evolution, because the real inner structure of the δ Scuti type primary may have different pulsational properties due to interior changes caused by the past mass transfer in the binary. Our preliminary analysis of these post-mass transfer δ Scuti stars suggests that they tend to be hotter and pulsate at higher frequencies than their single-evolution counterparts. The binary evolution scenario is a possible candidate to explain the overabundance of high-frequency δ Scuti pulsators (Balona et al. 2015). This will be presented in a separate paper (Z. Guo in prep.).

6. Evolution

The primary star of KIC 8262223 appears like a normal A-type dwarf near the zero age main sequence (ZAMS) (slightly over-luminous), while the low-mass secondary is noticeably oversized and over-luminous. The classical scenario for the formation of this type of cool Algol system involves the mass transfer (probably case B) from the original massive primary (donor) to the original less massive secondary, leading to a mass reversal (Paczynski 1971; Nelson & Eggleton 2001; Eggleton & Kiseleva- Eggleton 2002).

KIC 8262223 is likely to evolve into a typical EL CVn system, which consists of a normal A- or F-type dwarf and a low mass ($\approx 0.2M_{\odot}$) helium white dwarf precursor (pre-He WD). Maxted et al. (2014) presented 17 EL CVn systems discovered by the WASP survey. KIC 8262223 closely resembles the cool Algol system KIC 10661783 described by Southworth et al. (2011) and Lehmann et al. (2013). The latter authors also discussed several similar systems such as AS Eri (Mkrtychian et al. 2004) and V228 (Kaluzny et al.

2007). Sarna et al. (2008) found that a system with similar initial masses and slightly longer period ($M_{10} = 0.88M_{\odot}$, $M_{20} = 0.85M_{\odot}$, $P = 1.35\text{d}$) can evolve to the current state of V228 ($M_2 = 0.20M_{\odot}$, $M_1 = 1.51M_{\odot}$, $P = 1.15\text{d}$) through non-conservative case B mass transfer. For better comparison, we list the parameters of four systems KIC 8262223, KIC 10661783, AS Eri, and V228 in Table 6. All these binaries consist of a low mass secondary ($\approx 0.2M_{\odot}$) and may have similar evolutionary history as detailed below.

In Figure 9, We show the positions of the above four systems and the evolutionary tracks of He-WDs calculated by Driebe et al. (1999). The $\log g$ and T_{eff} of KIC 8262223 are fitted nicely by the evolutionary track of mass $0.195M_{\odot}$, matching the observed mass from RVs ($0.20 \pm 0.01M_{\odot}$). The observed quantities of other three systems also agree with the theory if the uncertainties of masses are considered.

Chen et al. (2016) found that EL CVn type binaries can result from non-conservative binary evolution with long-term stable mass transfer between low-mass stars and that avoided a rapid common-envelope evolution. They did thorough simulations with the MESA code (Paxton et al. 2011, 2013) to analyze the evolution channel of EL CVn stars from low mass progenitors ($M_{10} \in [0.9, 2.0]M_{\odot}$ and $q_0 = M_{10}/M_{20} \in [1.1, 4.0]$). The parameters of the secondary star of KIC 8262223 ($R_2/a = 0.176$, $T_{\text{eff}2} = 6849\text{K}$) fit their $R_2/a - T_{\text{eff}2}$ relation for pre-He WD very well (see their Fig. 9). They also found a tight correlation between orbital periods and WD masses as shown in their Figure 10. Our observed values ($P = 1.6\text{d}$, $M_2 = 0.20M_{\odot}$) also nicely match their theoretical relations. According to their Figure 7, the pre-He WD in KIC 8262223 with a mass of $0.2M_{\odot}$ has an envelope mass of $0.02M_{\odot}$.

To form EL CVn stars from two low mass progenitors, the initial orbital period has to be slightly longer than the ‘bifurcation period’ (P_b). The mass donor will evolve to cooler, less luminous part of the H-R diagram when mass transfer starts and eventually enter into a long-lived phase at nearly constant luminosity (pre-He WD phase). The donor in systems with shorter periods ($P < P_b$) will evolve to a state of very low luminosity and very short orbital period (on the order of 1 hr) (Chen et al. 2016).

Due to the uncertainties in the treatment of mass loss and angular momentum loss of binary evolution, we do not attempt to find a best matching evolution history for KIC 8262223. Instead, we show that this binary as well as other binaries in Table 6 can be qualitatively explained by the aforementioned formation channel. We used the binary module of MESA evolution code (v7624) and evolved two typical systems: (1) $M_{10} = 1.35M_{\odot}$, $M_{20} = 1.15M_{\odot}$ and $P_0 = 2.89\text{ d}$; (2) $M_{10} = 1.0M_{\odot}$, $M_{20} = 0.9M_{\odot}$ and $P_0 = 3.0\text{d}$. The metallicities were set to the solar value ($Z = 0.02$) and initial helium abundances were fixed to $Y = 0.28$. The evolutionary tracks were assumed to be non-conservative. Following the assumptions in Chen et al. (2016), half of the mass lost from the vicinity of the donor is accreted by the

gainer while the other 50% leaves the system as a fast wind, carrying away the same angular momentum of the donor. The mass transfer rate is calculated implicitly using the Ritter scheme (Ritter 1988).

The evolutionary paths are shown in the H-R diagram in Figure 10. The black and red tracks are for the donor and gainer in model (1), respectively. In Figure 11 we show the evolution of parameters of model (1). The system starts with an orbital period of 2.89 d, and the two stars follow their single star evolutionary tracks and the orbit slightly shrinks. The mass transfer begins when the primary evolves to the sub-giant stage and its radius reaches its Roche lobe (at $t = 3.32$ Gyr, marked by the filled circles). During the mass transfer, the radius of the donor is the same or slightly larger than the Roche lobe (to a few percent). The orbital period gets shorter further and the system shrinks until the two stars have equal masses ($t = 3.85$ Gyr, marked by the filled triangles), after which the orbit begins to expand. At an age of 4.18 Gyr as indicated by the filled stars, the mass transfer stops. At the same time, the radius of the donor star reaches a maximum, and it then begins to contract, cool, and evolve to a He WD precursor. The system ends up with parameter values $M_1 = 0.218M_\odot$, $M_2 = 1.716M_\odot$, and $P = 3.59$ d.

We also present the evolution of the initial primary and secondary star (gray and light red lines, respectively) of model (2) in Figure 10. The filled circles in gray and light red indicate the onset of mass transfer. The final status of this system has parameters of $M_1 = 0.20M_\odot$, $M_2 = 1.30M_\odot$, $P = 1.06$ d. The observed positions of the four systems mentioned above are also shown in the same Figure. The low mass secondary which was the previous mass donor is indicated by black open symbols. The mass gainers evolve along the red tracks to the upper left and arrive at the observed locations of the A- or F-type dwarfs (red open symbols). The evolutionary tracks of these two representative models are not meant to explain quantitatively the properties of the four systems, but rather to show the regions that the product of the binary evolution can occupy on the H-R diagram and the final status for the formation of EL CVn stars. For KIC 8262223, the secondary seems to be a star that has just finished its mass transfer and is contracting (i.e., from filling its Roche lobe to under-filling its Roche lobe). It may evolve into an EL CVn star after some further contraction.

It is interesting to note that the dwarf stars in these systems are often pulsating (all but V228, which has a mass too low to be a δ Scuti pulsator). As can be seen in Table 6, these systems can pulsate at low ($20 - 30$ d $^{-1}$) as well as high frequencies ($50 - 60$ d $^{-1}$). It is known that the unstable range of pulsations will vary as the star evolves off the ZAMS. For example, for a δ Scuti star with $M = 1.8M_\odot$, the p -modes $n_p = 4 - 7$ ($45 - 60$ d $^{-1}$) are unstable for young models close to ZAMS. The unstable range moves to $5 - 25$ d $^{-1}$ for models

near TAMS which are low order p-modes or g-modes (Dupret 2002). Asteroseismology has the potential of determining the ages of the δ Scuti pulsators in these EL CVn binaries. Not only the dwarfs, but the pre-He WD precursor can also show pulsations. One such example is the g -mode pulsating WD in KIC 9164561 (Zhang et al. 2016). Such pulsations enabled the discovery of a thick hydrogen envelope on the pre-He WD J0247-25B (Maxted et al. 2013). The theoretical instability strip of these pre-He WDs has been examined closely by Córscico & Althaus (2016). More information can be extracted from these pulsations, which may lead to great advancements in our understanding of the evolution of low mass close binaries.

7. Conclusions and Prospects

Utilizing the accurate *Kepler* photometric data and our ground-based spectroscopic data, we determined the fundamental parameters of KIC 8262223, an eclipsing binary system with an orbital period of 1.6 days which contains an A-type dwarf and a low mass pre-He WD. The light curves show high frequency pulsations at about 60 d^{-1} . These δ Scuti type pulsations are likely from the primary star and can be explained as radial and non-radial p-modes. We discussed possible evolutionary scenarios and showed that this system and several other very similar binaries can be explained by the non-conservative evolution of close binaries with low mass progenitors, the channel that forms EL CVn type stars. KIC 8262223 also poses some challenges to our non-adiabatic theory of stellar pulsations as the modes calculated from the equilibrium model which match the observed modes of the primary are stable. A future spectroscopic follow up covering the full orbit could help pinpoint accurate masses and rotational alignment.

Asteroseismic modeling has not yet been applied to δ Scuti stars in pulsating Algols (oEAs) due to the complex nature of these systems. As a prerequisite, it is possible to identify the pulsation modes through high cadence and high resolution spectroscopy. The eclipse mapping method (Reed et al. 2005; Bíró & Nuspl 2011) is also promising but still awaits application to a real object. Several hundreds of δ Scuti variables are already detected by the *Kepler* satellite, and future missions like *TESS* will provide more systems. A complete analysis of their pulsational properties will require a better understanding of close binary tidal interactions and binary evolution.

We thank Jerome A. Orosz for his constant support in using the ELC code. We thank Bill Paxton, Rich Townsend and others for maintaining and updating MESA and GYRE. We thank Meng Sun for helpful discussions. This work is partly based on data from the *Kepler*

mission. Funding for this mission is provided by NASA’s Science Mission Directorate. The photometric data were obtained from the Mikulski Archive for Space Telescopes (MAST). STScI is operated by the Association of Universities for Research in Astronomy, Inc., under NASA contract NAS5-26555. This study was supported by NASA grants NNX12AC81G, NNX13AC21G, and NNX13AC20G. This material is based upon work supported by the National Science Foundation under Grant No. AST-1411654. A. G. H. acknowledges support from Fundação para a Ciência e a Tecnologia (FCT, Portugal) through the fellowship SFRH/ BPD/80619/2011, and from the EC Project SPACEINN (FP7-SPACE-2012-312844). Z. H. is partly supported by the Natural Science Foundation of China (Grant Nos 11521303, 11390374). Institutional support has been provided from the GSU College of Arts and Sciences and the Research Program Enhancement fund of the Board of Regents of the University System of Georgia, administered through the GSU Office of the Vice President for Research and Economic Development.

REFERENCES

- Aerts, C., Christensen-Dalsgaard, J., & Kurtz, D. W. 2010, *Asteroseismology*, Astronomy and Astrophysics Library (Heidelberg: Springer)
- Armstrong, D. J., Gomez Maqueo Chew, Y., Faedi, F., & Pollacco, D. 2014, *MNRAS*, 437, 3473
- Bagnuolo, W. G., Jr., Gies, D. R., Hahula, M. E., Wiemker, R., & Wiggs, M. S. 1994, *ApJ*, 423, 446
- Balona, L. A., Daszyńska-Daszkiewicz, J., & Pamyatnykh, A. A. 2015, *MNRAS*, 452, 3073
- Bíró, I. B., & Nuspl, J. 2011, *MNRAS*, 416, 1601
- Charbonneau, P. 1995, *ApJS*, 101, 309
- Chen, X., Maxted, P. F. L., Li, J., & Han, Z., *MNRAS*, submitted, arXiv:1604.01956
- Conroy, K. E., Prša, A., Stassun, K. G., et al. 2014, *AJ*, 147, 45
- Córsico, A. H., & Althaus, L. G. 2016, *A&A*, 585, A1
- da Silva, R., Maceroni, C., Gandolfi, D., Lehmann, H., & Hatzes, A. P. 2014, *A&A*, 565, A55
- Driebe, T., Bloeker, T., Schönberner, D., & Herwig, F. 1999, *A&A*, 350, 89
- Dupret, M. A. 2002, *Bulletin de la Société Royale des Sciences de Liège*, 71, 249
- Eggleton, P. P., & Kiseleva-Eggleton, L. 2002, *ApJ*, 575, 461
- García Hernández, A., Martín-Ruiz, S., Monteiro, M. J. P. F. G., et al. 2015, *ApJ*, 811, L29
- Gies, D. R., Williams, S. J., Matson, R. A., et al. 2012, *AJ*, 143, 137
- Gies, D. R., Matson, R. A., Guo, Z., et al. 2015, *AJ*, 150, 178
- Grevesse, N., & Sauval, A. J. 1998, *Space Sci. Rev.*, 85, 161
- Groot, P. J. 2012, *ApJ*, 745, 55
- Guo, Z, Gies, D. R., Matson, R. A., et al. 2016, *ApJ*, 826, 69
- Hambleton, K. M., Kurtz, D. W., Prsa, A., et al. 2013, *MNRAS*, 434, 925

- Hensberge, H., Ilijić, S., & Torres, K. B. V. 2008, *A&A*, 482, 1031
- Iglesias, C. A., & Rogers, F. J. 1996, *ApJ*, 464, 943
- Ilijic, S., Hensberge, H., Pavlovski, K., & Freyhammer, L. M. 2004, (ASP Conf. Vol. 318), ed. R. W. Hilditch, H. Hensberge, & K. Pavlovski, (San Francisco: ASP), 111
- Kallinger, T., Reegen, P., & Weiss, W. W. 2008, *A&A*, 481, 571
- Kaluzny, J., Thompson, I. B., Rucinski, S. M., et al. 2007, *AJ*, 134, 541
- Lehmann, H., Southworth, J., Tkachenko, A., & Pavlovski, K. 2013, *A&A*, 557, A79
- Lenz, P., & Breger, M. 2005, *Communications in Asteroseismology*, 146, 53
- Maceroni, C., Lehmann, H., da Silva, R., et al. 2014, *A&A*, 563, A59
- Matson, R. A., Gies, D. R., Guo, Z., & Orosz, J. A. 2016, *AJ*, 151, 139
- Maxted, P. F. L., Serenelli, A. M., Miglio, A., et al. 2013, *Nature*, 498, 463
- Maxted, P. F. L., Bloemen, S., Heber, U., et al. 2014, *MNRAS*, 437, 1681
- Mkrtychian, D. E., Kusakin, A. V., Gamarova, A. Y., et al. 2002, in *Observational Aspects of Pulsating B- and A Stars*, (ASP Conf. Vol. 256), ed. C. Sterken & D. W. Kurtz (San Francisco: ASP), 259
- Mkrtychian, D. E., Nazarenko, V., Gamarova, A. Y., et al. 2003, in *Interplay of Periodic, Cyclic and Stochastic Variability in Selected Areas of the H-R Diagram*, (ASP Conf. Vol. 292), ed. C. Sterken (San Francisco: ASP), 113
- Mkrtychian, D. E., Kusakin, A. V., Rodriguez, E., et al. 2004, *A&A*, 419, 1015
- Nelson, C. A., & Eggleton, P. P. 2001, *ApJ*, 552, 664
- Orosz, J. A., & Hauschildt, P. H. 2000, *A&A*, 364, 265
- Paczynski, B. 1971, *ARA&A*, 9, 183
- Paparo, M., Benkő, J. M., Hareter, M., & Guzik, J. A. 2016a, *ApJ*, 822, 100
- Paparo, M., Benkő, J. M., Hareter, M., & Guzik, J. A. 2016b, *ApJS*, 224, 41
- Paxton, B., Bildsten, L., Dotter, A., et al. 2011, *ApJS*, 192, 3
- Paxton, B., Cantiello, M., Arras, P., et al. 2013, *ApJS*, 208, 4

- Prša, A., Batalha, N., Slawson, R. W., et al. 2011, *AJ*, 141, 83
- Reed, M. D., Brondel, B. J., & Kawaler, S. D. 2005, *ApJ*, 634, 602
- Ritter, H. 1988, *A&A*, 202, 93
- Rodríguez-Merino, L. H., Chavez, M., Bertone, E., & Buzzoni, A. 2005, *ApJ*, 626, 411
- Sarna, M. J. 2008, arXiv:0812.5051
- Slawson, R. W., Prša, A., Welsh, W. F., et al. 2011, *AJ*, 142, 160
- Southworth, J., Zima, W., Aerts, C., et al. 2011, *MNRAS*, 414, 2413
- Soydugan, E., Soydugan, F., Demircan, O., & İbanoğlu, C. 2006, *MNRAS*, 370, 2013
- Stellingwerf, R. F. 1978, *AJ*, 83, 1184
- Suárez, J. C., García Hernández, A., Moya, A., et al. 2014, *A&A*, 563, A7
- Telting, J. H., Østensen, R. H., Baran, A. S., et al. 2012, *A&A*, 544, A1
- Townsend, R. H. D., & Teitler, S. A. 2013, *MNRAS*, 435, 3406
- van Kerkwijk, M. H., Rappaport, S. A., Breton, R. P., et al. 2010, *ApJ*, 715, 51
- Zhang, X. B., Fu, J. N., Li, Y., et al. 2016, *ApJ*, 821, L32

Table 1. Radial Velocities

Time (BJD-2400000)	Phase	$V_r(\text{pri})$ (km s ⁻¹)	$O - C$ (km s ⁻¹)	$V_r(\text{sec})$ (km s ⁻¹)	$O - C$ (km s ⁻¹)	Observation Source
55369.9232	0.19	1.5 ± 1.7	-0.9	215.4 ± 4.3	0.4	KPNO
55732.8574	0.19	2.6 ± 1.7	0.4	213.5 ± 4.5	-3.3	KPNO
55815.8979	0.68	42.7 ± 1.9	0.2	-159.2 ± 5.9	-2.1	KPNO
56077.9534	0.14	6.2 ± 1.7	0.8	185.0 ± 4.7	4.2	KPNO
56078.7629	0.64	42.3 ± 2.4	2.0	-144.2 ± 7.0	-11.9	KPNO
56078.8440	0.79	42.0 ± 1.8	-1.2	-163.3 ± 5.7	1.9	KPNO
56078.9357	0.75	45.8 ± 1.9	1.6	-183.5 ± 5.6	-3.9	KPNO
56079.7925	0.28	9.3 ± 3.4	7.2	220.4 ± 10.7	-6.4	KPNO
56081.9642	0.63	34.8 ± 2.9	-4.2	-103.3 ± 6.4	15.5	KPNO
56082.8204	0.16	3.1 ± 1.8	-1.0	195.2 ± 4.7	0.9	KPNO
56082.8833	0.20	1.7 ± 1.7	-0.4	217.2 ± 4.7	0.0	KPNO
56082.9468	0.23	0.6 ± 2.0	-0.8	227.5 ± 5.6	-1.2	KPNO

Table 2. Orbital Parameters

Parameter	RVs	Spectral Disentangling
T_0 (primary minimum) (HJD-2,400,000)	55690.5 ± 0.1	55690.605
K_1 (km s ⁻¹)	21.4 ± 1.0	21.5
K_2 (km s ⁻¹)	204.8 ± 3.2	201.4
γ_1 (km s ⁻¹)	22.8 ± 0.6	...
γ_2 (km s ⁻¹)	25.1 ± 1.7	...
e	0.0 ^a	0.0 ^a
rms_1 (km s ⁻¹)	2.6	...
rms_2 (km s ⁻¹)	6.3	...

^aFixed.

Table 3. Atmospheric Parameters

Parameter	Primary	Secondary
T_{eff} (K)	9128 ± 130	7119 ± 150
$\log g$ (cgs)	4.3 ^a	3.5 ^a
$v \sin i$ (km s ⁻¹) ...	37 ± 13	35 ± 10
[Fe/H]	-0.05 ± 0.10	-0.05 ± 0.10
Flux Contribution	82.6%	17.4%

^aFixed.

Table 4. Model Parameters

Parameter	Solution
Period (days)	1.61301476 ^a
Time of primary minimum (HJD-2400000)	55432.522844 ± 0.000007
Mass ratio $q = M_2/M_1$	0.104 ± 0.002
Orbital eccentricity e	0.0 ^a
Orbital inclination i (degree)	75.203 ± 0.007
Semi-major axis a (R_\odot)	7.45 ± 0.11
M_1 (M_\odot)	1.94 ± 0.06
M_2 (M_\odot)	0.20 ± 0.01
R_1 (R_\odot)	1.67 ± 0.03
R_2 (R_\odot)	1.31 ± 0.02
Filling factor f_1	0.314 ± 0.003
Filling factor f_2	0.672 ± 0.001
Gravity brightening, β_1	0.25 ^a
Gravity brightening, β_2	0.08 ^a
Bolometric albedo 1	1.0 ^a
Bolometric albedo 2	0.22
Beaming parameter 1	2.76 ^a
Beaming parameter 2	3.48 ^a
T_{eff1} (K)	9128 ^a
T_{eff2} (K)	6849 ± 15
$\log g_1$ (cgs)	4.28 ± 0.04
$\log g_2$ (cgs)	3.51 ± 0.06
Synchronous $v \sin i_1$ (km s ⁻¹)	50.6 ± 0.9
Synchronous $v \sin i_2$ (km s ⁻¹)	39.6 ± 0.6

^aFixed.

Table 5. Significant oscillation frequencies

	Frequency (d^{-1})	Amplitude (10^{-3})	Phase ($\text{rad}/2\pi$)	S/N	Comment
f_1	64.43390 ± 0.00010	1.319 ± 0.020	0.896 ± 0.007	114.5	
f_2	57.17794 ± 0.00016	0.918 ± 0.022	0.313 ± 0.011	72.3	
f_3	61.43616 ± 0.00018	0.782 ± 0.021	0.190 ± 0.012	64.4	
f_4	53.64792 ± 0.00024	0.620 ± 0.022	0.345 ± 0.016	49.0	
f_5	51.04548 ± 0.00026	0.565 ± 0.021	0.281 ± 0.017	46.0	
f_6	54.78183 ± 0.00028	0.540 ± 0.022	0.368 ± 0.019	42.5	
f_7	63.28439 ± 0.00028	0.497 ± 0.020	0.516 ± 0.019	42.2	
f_8	60.31265 ± 0.00040	0.366 ± 0.021	0.949 ± 0.027	29.7	
f_9	61.19863 ± 0.00040	0.363 ± 0.021	0.896 ± 0.027	29.8	
f_{10}	49.08047 ± 0.00039	0.357 ± 0.020	0.218 ± 0.027	30.1	
f_{11}	60.19302 ± 0.00052	0.284 ± 0.021	0.669 ± 0.035	22.9	
f_{12}	63.82187 ± 0.00049	0.281 ± 0.020	0.947 ± 0.033	24.1	
f_{13}	54.88585 ± 0.00059	0.255 ± 0.022	0.607 ± 0.040	20.0	
f_{14}	62.43309 ± 0.00063	0.226 ± 0.020	0.717 ± 0.042	18.9	
f_{15}	53.54042 ± 0.00071	0.212 ± 0.022	0.134 ± 0.048	16.7	
f_{16}	57.77610 ± 0.00071	0.210 ± 0.022	0.885 ± 0.048	16.6	
f_{17}	50.32422 ± 0.00071	0.201 ± 0.021	0.513 ± 0.048	16.6	
f_{18}	55.94001 ± 0.00078	0.193 ± 0.022	0.050 ± 0.053	15.2	
f_{19}	50.97786 ± 0.00079	0.185 ± 0.021	0.755 ± 0.053	15.1	
f_{21}	64.47378 ± 0.00079	0.172 ± 0.020	0.584 ± 0.053	14.9	
f_{22}	61.55406 ± 0.00086	0.167 ± 0.021	0.746 ± 0.058	13.7	
f_{23}	61.46043 ± 0.00087	0.165 ± 0.021	0.255 ± 0.059	13.6	
f_{24}	58.42108 ± 0.00097	0.153 ± 0.022	0.494 ± 0.066	12.2	
f_{25}	63.66929 ± 0.00096	0.144 ± 0.020	0.252 ± 0.065	12.3	
f_{26}	49.85027 ± 0.00100	0.143 ± 0.021	0.713 ± 0.067	11.9	
f_{27}	58.42454 ± 0.00108	0.138 ± 0.022	0.593 ± 0.073	10.9	
f_{28}	60.23810 ± 0.00108	0.135 ± 0.021	0.568 ± 0.073	10.9	
f_{29}	59.09553 ± 0.00117	0.127 ± 0.021	0.757 ± 0.079	10.1	
f_{30}	56.62486 ± 0.00120	0.126 ± 0.022	0.992 ± 0.081	9.9	
f_{31}	60.28838 ± 0.00126	0.116 ± 0.021	0.751 ± 0.085	9.4	
f_{32}	64.52926 ± 0.00119	0.114 ± 0.020	0.752 ± 0.080	9.9	
f_{33}	52.27648 ± 0.00130	0.114 ± 0.021	0.204 ± 0.088	9.1	

Table 5—Continued

	Frequency (d ⁻¹)	Amplitude (10 ⁻³)	Phase (rad/2 π)	S/N	Comment
f_{34}	50.42825 \pm 0.00130	0.111 \pm 0.021	0.808 \pm 0.088	9.1	
f_{35}	54.50442 \pm 0.00142	0.105 \pm 0.022	0.515 \pm 0.096	8.3	
f_{36}	63.20290 \pm 0.00146	0.096 \pm 0.020	0.717 \pm 0.099	8.1	
f_{37}	56.85719 \pm 0.00165	0.091 \pm 0.022	0.197 \pm 0.111	7.2	
f_{38}	59.76651 \pm 0.00174	0.084 \pm 0.021	0.690 \pm 0.118	6.8	
f_{40}	57.75009 \pm 0.00199	0.075 \pm 0.022	0.430 \pm 0.134	5.9	
f_{41}	61.62167 \pm 0.00207	0.069 \pm 0.021	0.177 \pm 0.139	5.7	
f_{42}	60.36814 \pm 0.00215	0.068 \pm 0.021	0.742 \pm 0.145	5.5	
f_{43}	51.07405 \pm 0.00215	0.068 \pm 0.021	0.854 \pm 0.145	5.5	
f_{44}	64.40949 \pm 0.00205	0.067 \pm 0.020	0.325 \pm 0.138	5.8	
f_{45}	61.36160 \pm 0.00222	0.065 \pm 0.021	0.574 \pm 0.150	5.3	
f_{46}	65.66649 \pm 0.00212	0.063 \pm 0.019	0.513 \pm 0.143	5.6	
f_{47}	66.96511 \pm 0.00209	0.062 \pm 0.019	0.258 \pm 0.141	5.7	
f_{48}	54.37597 \pm 0.00243	0.062 \pm 0.022	0.028 \pm 0.164	4.9	
f_{49}	51.11913 \pm 0.00237	0.061 \pm 0.021	0.195 \pm 0.160	5.0	
f_{50}	60.16181 \pm 0.00242	0.060 \pm 0.021	0.567 \pm 0.163	4.9	
f_{51}	60.34386 \pm 0.00242	0.060 \pm 0.021	0.157 \pm 0.163	4.9	
f_{52}	58.97922 \pm 0.00247	0.060 \pm 0.021	0.686 \pm 0.167	4.8	
f_{54}	55.81344 \pm 0.00262	0.057 \pm 0.022	0.227 \pm 0.177	4.5	
f_{55}	58.14367 \pm 0.00266	0.056 \pm 0.022	0.960 \pm 0.179	4.5	
f_{56}	59.80451 \pm 0.00275	0.054 \pm 0.021	0.532 \pm 0.185	4.3	
f_{58}	0.79928 \pm 0.00277	0.052 \pm 0.021	0.658 \pm 0.187	4.3	
f_{59}	54.28582 \pm 0.00294	0.051 \pm 0.022	0.767 \pm 0.199	4.0	
f_{60}	48.03643 \pm 0.00270	0.051 \pm 0.020	0.140 \pm 0.182	4.4	
f_{61}	59.63633 \pm 0.00291	0.051 \pm 0.021	0.109 \pm 0.197	4.1	
f_{62}	62.25437 \pm 0.00288	0.049 \pm 0.021	0.425 \pm 0.194	4.1	
f_{63}	64.90535 \pm 0.00281	0.048 \pm 0.020	0.340 \pm 0.190	4.2	
f_{64}	65.72024 \pm 0.00282	0.047 \pm 0.019	0.585 \pm 0.190	4.2	
f_{20}	1.23967 \pm 0.00079	0.183 \pm 0.021	0.027 \pm 0.053	14.9	$2f_{orb}$
f_{39}	58.09686 \pm 0.00194	0.077 \pm 0.022	0.993 \pm 0.131	6.1	$f_{37} + 2f_{orb}$
f_{53}	49.18796 \pm 0.00242	0.058 \pm 0.020	0.677 \pm 0.163	4.9	$f_{34} - 2f_{orb}$
f_{57}	62.58379 \pm 0.00267	0.053 \pm 0.020	0.528 \pm 0.180	4.4	$f_{36} - f_{orb}$

Table 6. Comparison of four cool Algols

Name	M_1 (M_\odot)	M_2 (M_\odot)	R_1 (R_\odot)	R_2 (R_\odot)	$T_{\text{eff}1}$ (K)	$T_{\text{eff}2}$ (K)	Period (days)	Pulsation (d^{-1})	Remark
KIC8262223	1.94	0.20	1.67	1.31	9128	6849	1.61	50 – 65	detached
KIC10661783	2.05	0.20	2.56	1.12	7760	5980	1.23	20 – 30	detached
AS Eri	1.92	0.21	1.50	1.15	7290	4250	2.66	≈ 60	semi-detached
V228	1.51	0.20	1.36	1.24	8070	5810	1.15	...	semi-detached

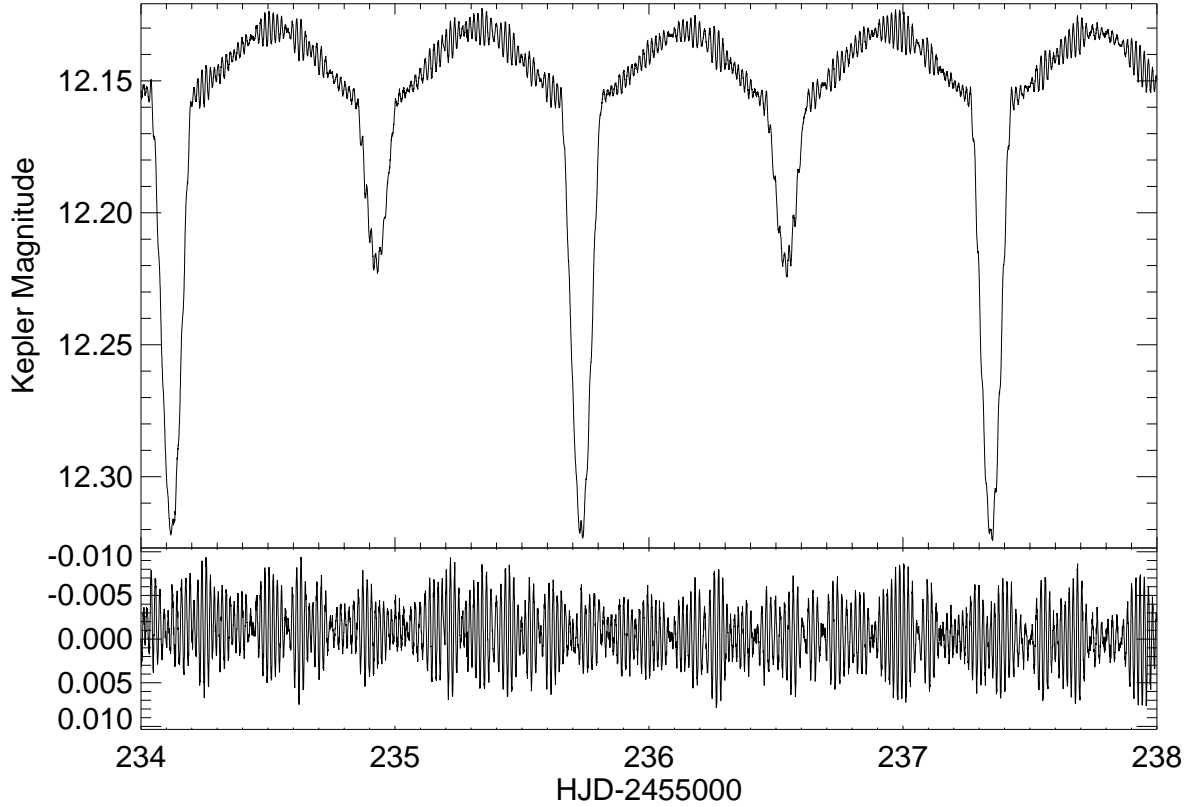


Fig. 1.— The de-trended short cadence light curve of KIC 8262223 during Quarter 4. The lower panel shows the residuals after subtracting the best binary light curve model.

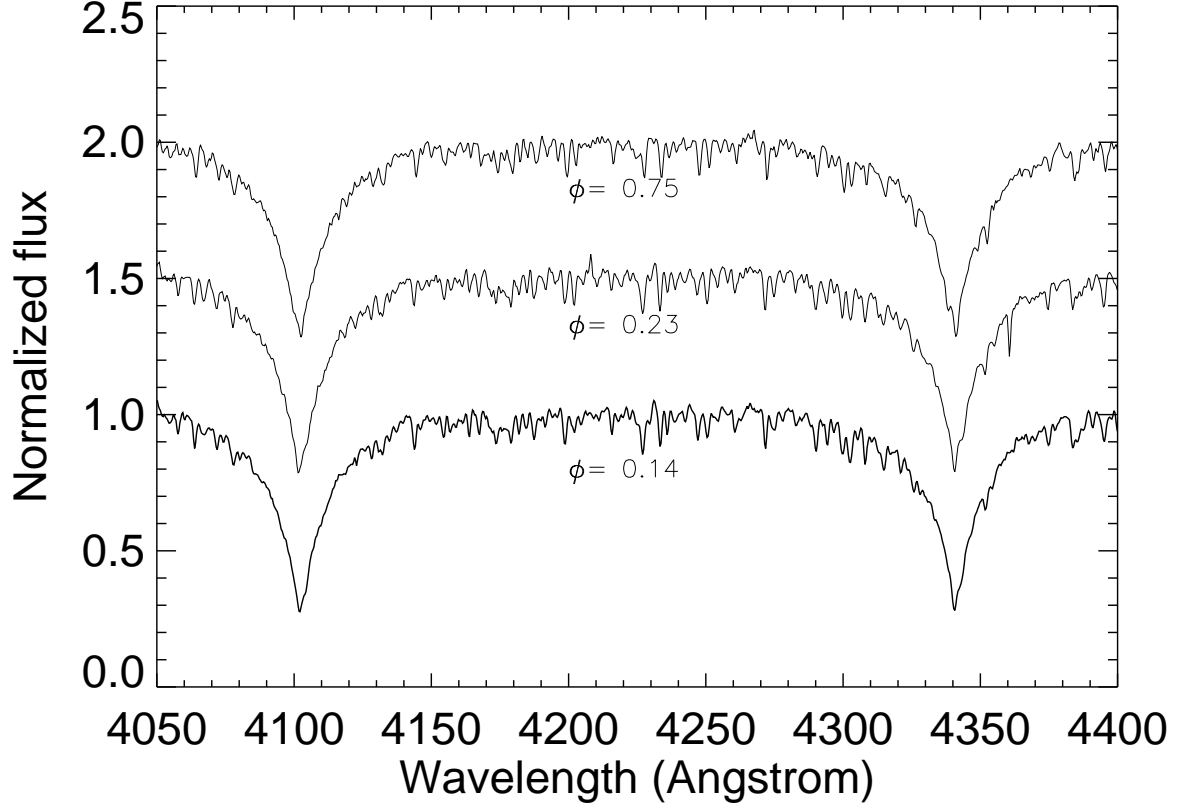


Fig. 2.— The observed composite spectra of KIC 8262223. For clarity, the spectra at orbital phases $\phi = 0.23$ and 0.75 have been shifted upwards by 0.5 and 1.0 , respectively. The Doppler shifts of the two components can be seen in the core of Balmer lines ($H\delta$ $\lambda 4102$ Å and $H\gamma$ $\lambda 4341$ Å).

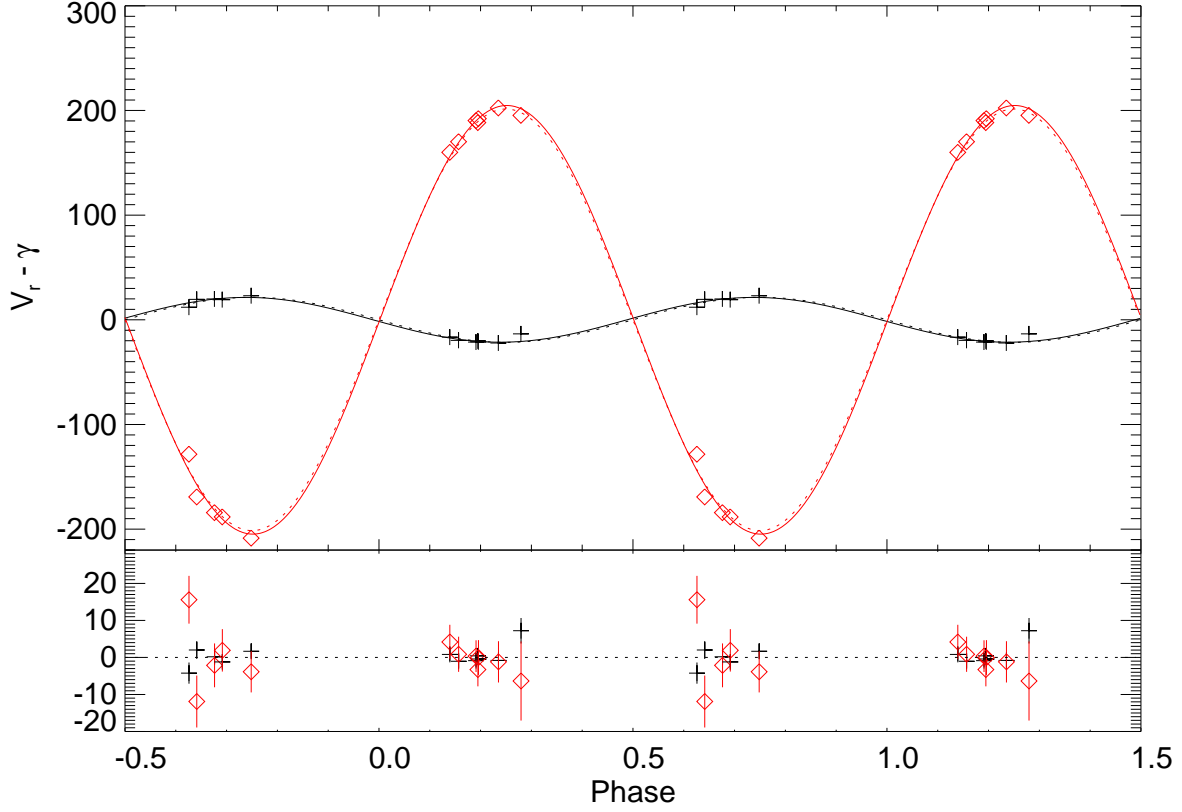


Fig. 3.— Radial velocities (RVs) in km s^{-1} and circular orbital solutions of KIC 8262223. The observed RVs of the primary and the secondary star from cross correlation are shown as black crosses and red diamonds, respectively. The black and red solid lines are the best-fit radial velocity curves for the primary and secondary, respectively. The lower panel shows the corresponding residuals. The RV models from the spectral disentangling technique by FDBinary are indicated as black and red dashed lines.

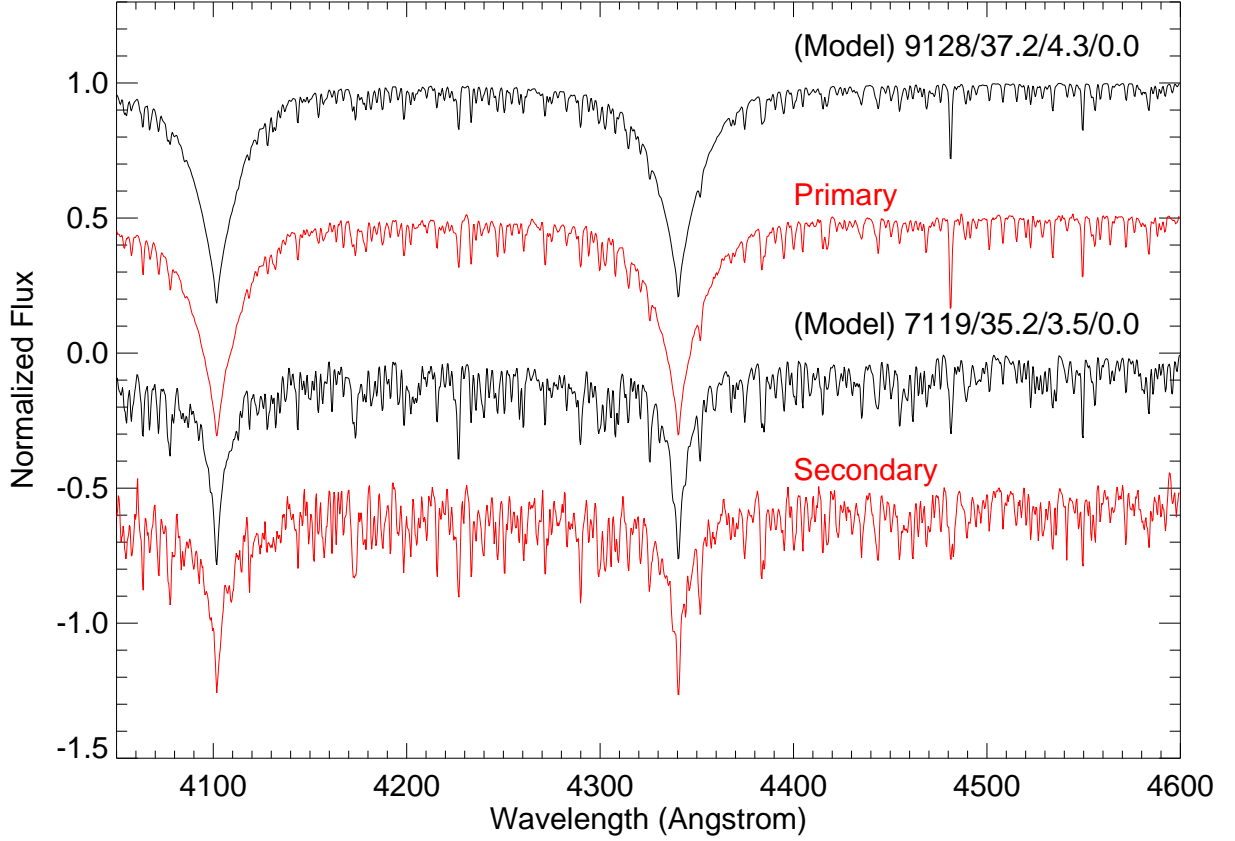


Fig. 4.— The reconstructed individual spectra (red) of the primary (upper) and secondary (lower) of KIC 8262223. The best matching atmospheric models from UVBLUE are shown as black spectra, and the corresponding parameters T_{eff} (K), $v \sin i$ (km s^{-1}), $\log g$ (cgs) and $[\text{Fe}/\text{H}]$ are labeled.

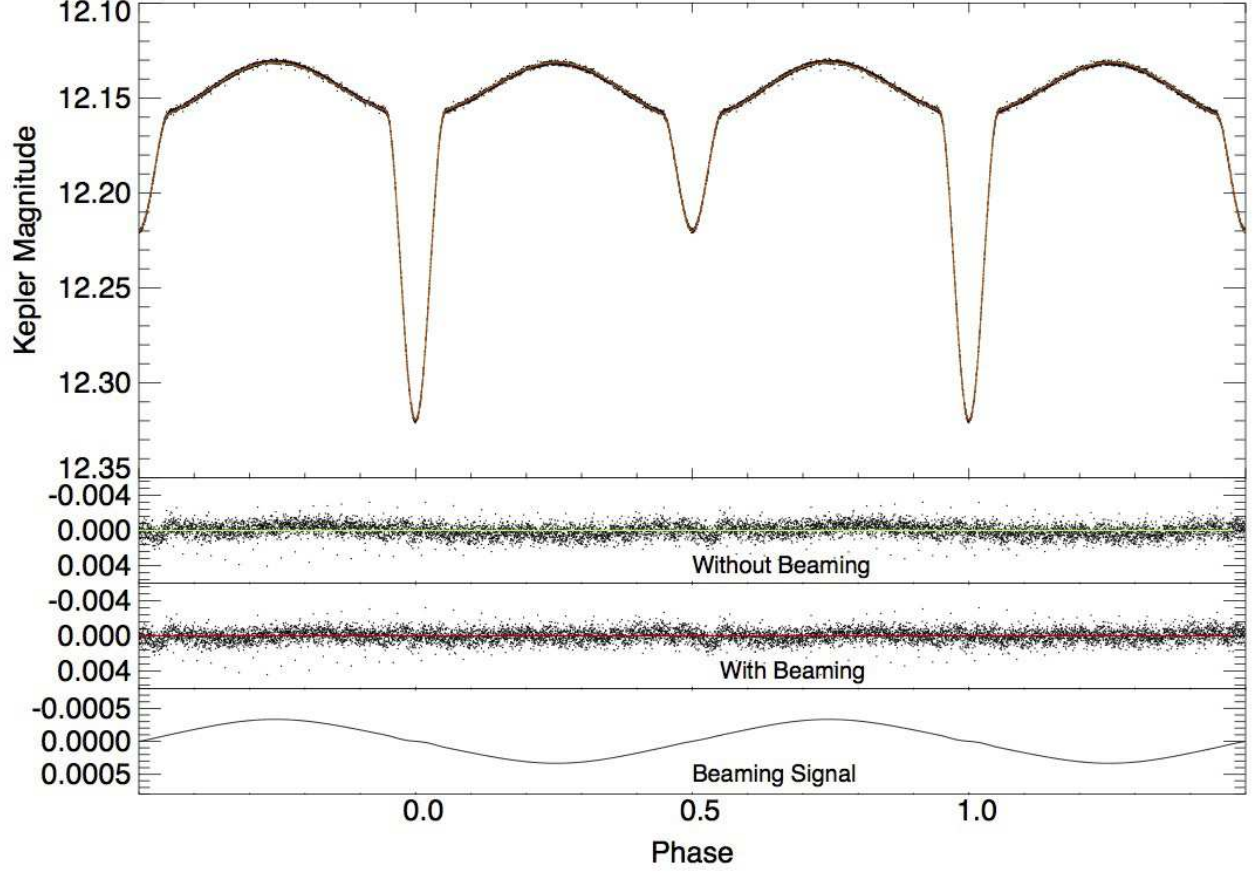


Fig. 5.— **Top panel:** The phase-folded long cadence light curve of KIC 8262223 (dots) in Quarter 4 and 5 and the best-fit model from ELC (red and green solid line) when the bolometric albedo of the secondary star (l_2) is allowed to vary. **Middle two panels:** The corresponding residuals without and with the Doppler beaming effect taken into account. **Bottom panel:** ELC model of the beaming lightcurve.

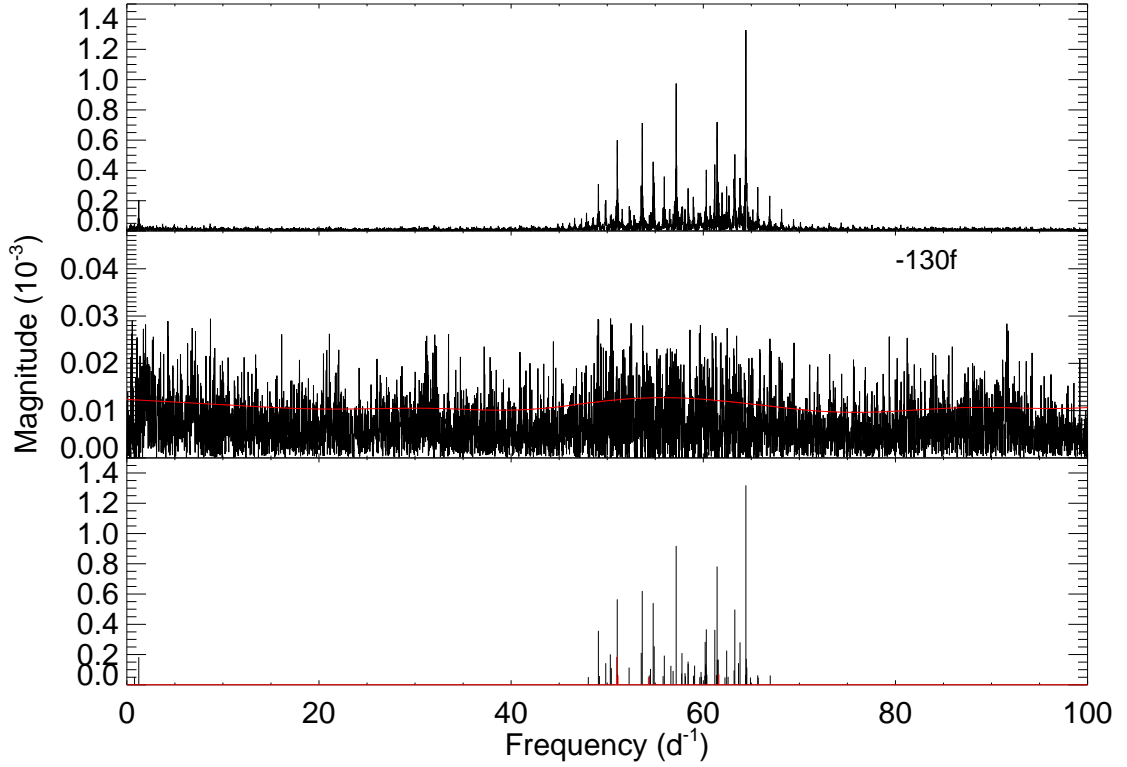


Fig. 6.— **Top panel:** The amplitude spectrum of the residual light curve of short cadence data (Q4) with eclipses masked. **Middle panel:** The noise spectrum after subtracting 130 frequencies. The solid red curve represents the adopted noise level. **Bottom panel:** The 64 extracted significant frequencies with $S/N > 4.0$ as listed in Table 5 (black: independent frequencies; red: combination frequencies).

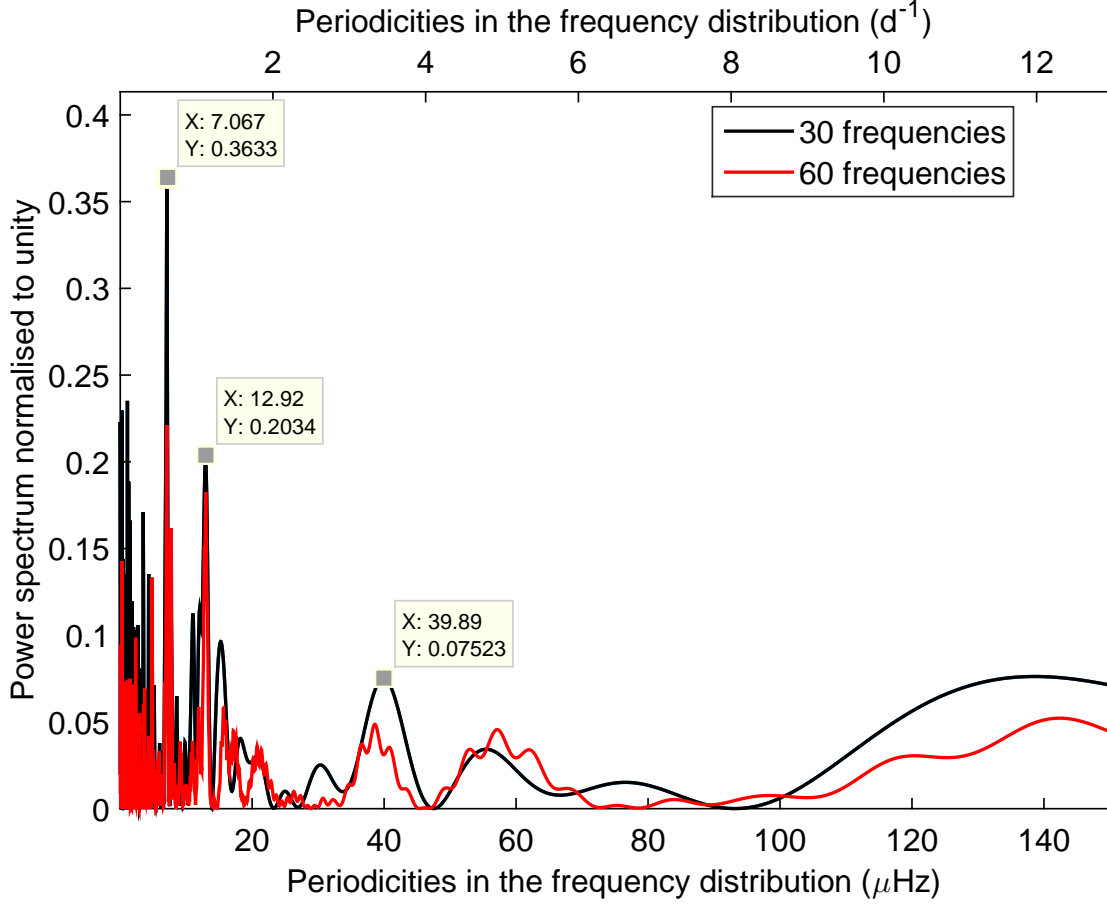


Fig. 7.— The Fourier spectrum of the reported oscillation frequencies in Table 5. The black and red lines are the results of using 30 and 60 highest frequencies, respectively. The highest peak at $7.067\mu\text{Hz}$ is likely the result of rotational splitting. The pattern at $39.89\mu\text{Hz}$ is related to half of the large frequency separation $\Delta\nu$. Please see text for more details.

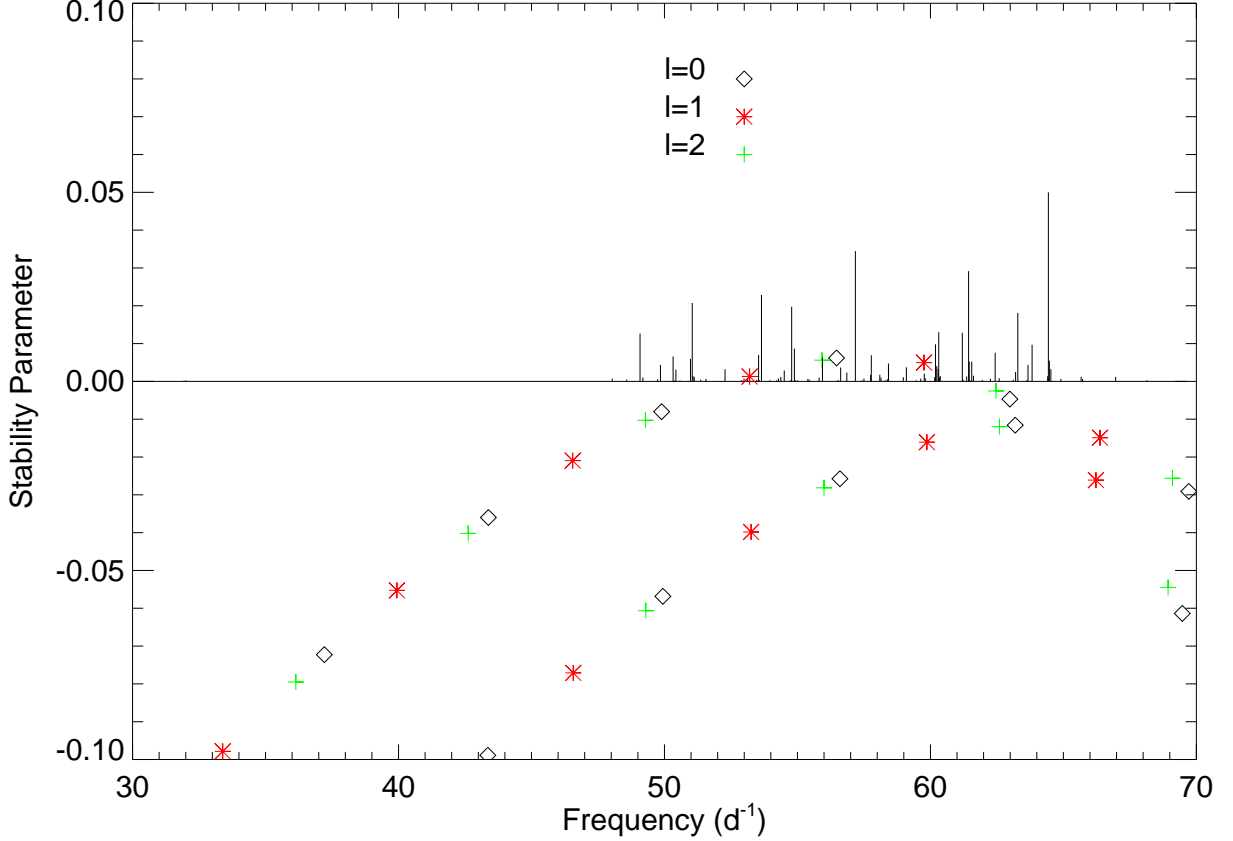


Fig. 8.— The stability parameter η of p-modes ($l = 0, 1, 2$) of two models for the primary star calculated with MESA and GYRE. The equilibrium models have the following parameters: (a) $M_1 = 1.79M_\odot$, $R_1 = 1.66R_\odot$; (b) $M_1 = 1.94M_\odot$, $R_1 = 1.67R_\odot$. Both models have the same $Z = 0.02$ and $Y = 0.28$, and Model (b) matches the observed fundamental parameters of KIC 8262223 primary. Modes of Model (a) are unstable (positive stability parameters) in the frequency range 53 – 62 d⁻¹ and all modes of model (b) are stable. The observed frequencies of KIC 8262223 are over-plotted and re-scaled for clarity.

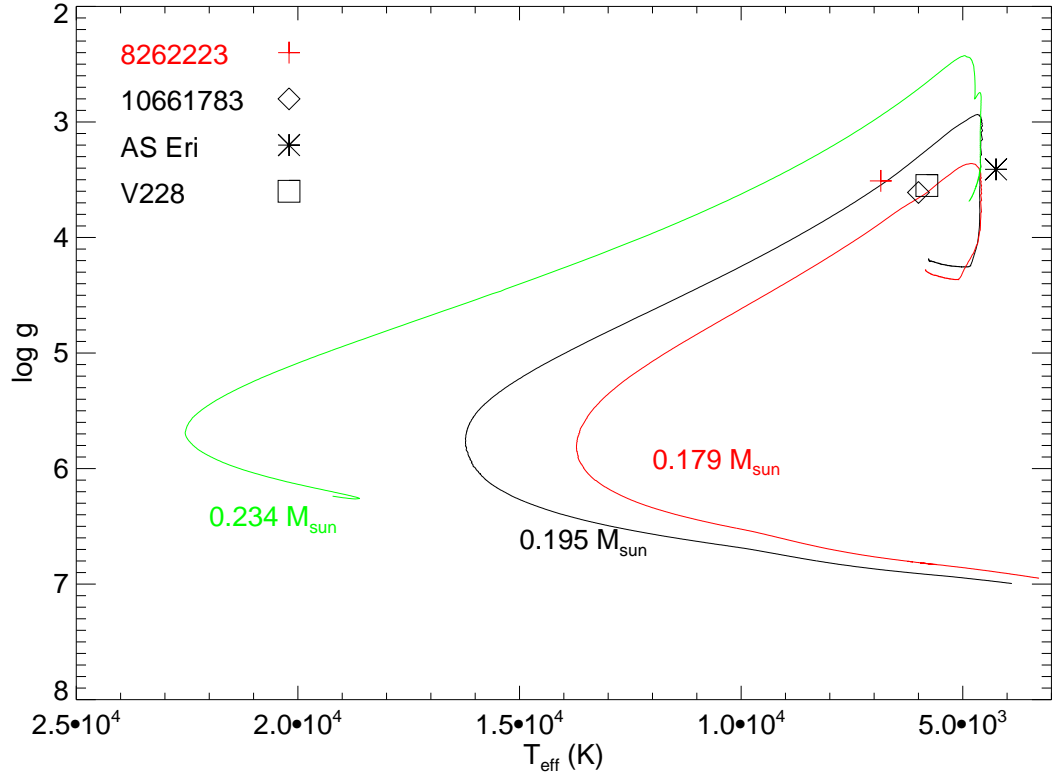


Fig. 9.— The evolutionary tracks of He-WDs calculated by Driebe et al. (1999). Three different masses are shown here ($0.179 M_{\odot}$, $0.195 M_{\odot}$, $0.234 M_{\odot}$). The four Algol systems discussed in text are over-plotted.

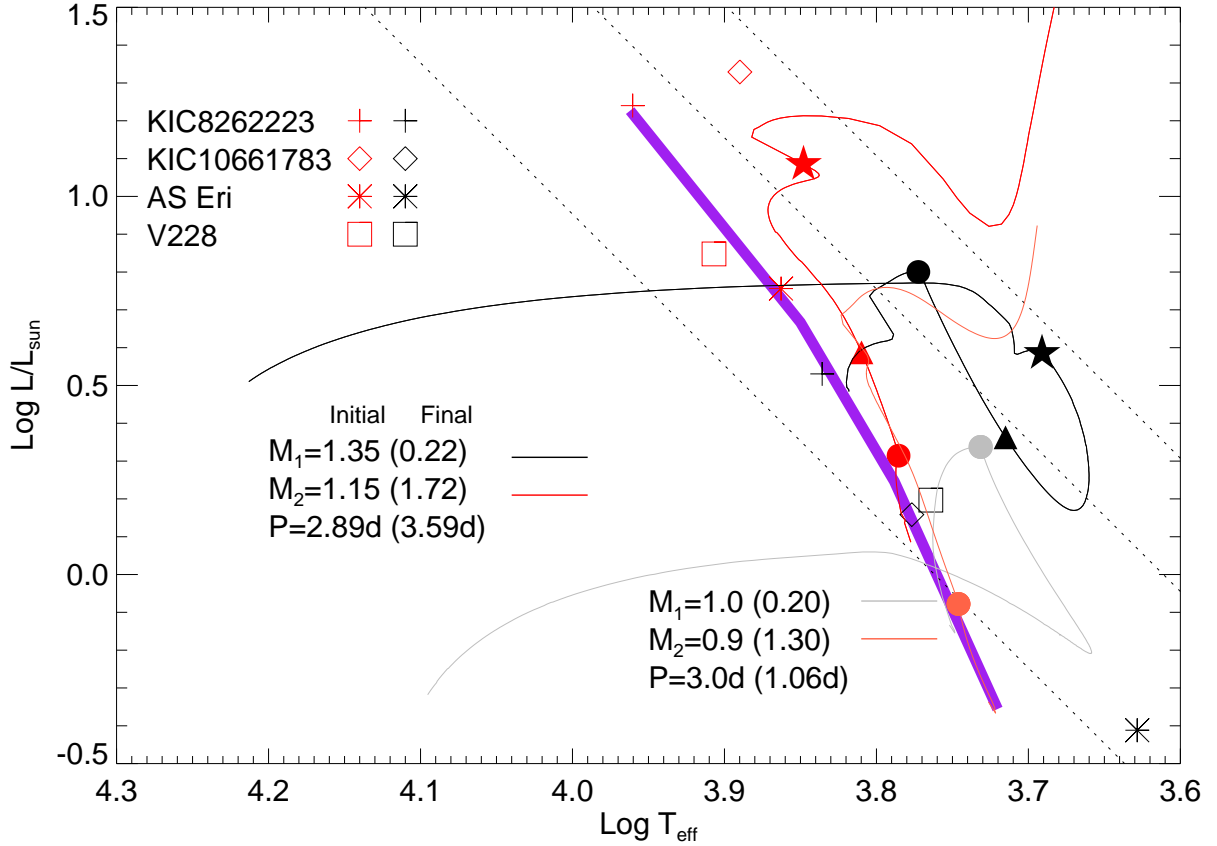


Fig. 10.— Evolutionary tracks for two binary models on the H-R diagram. Model (1) has initial parameters: $M_{10} = 1.35M_{\odot}$, $M_{20} = 1.15M_{\odot}$, $P = 2.89\text{d}$ and final parameters: $M_1 = 0.22M_{\odot}$, $M_2 = 1.72M_{\odot}$, $P = 3.59\text{d}$. Model (2) has initial parameters: $M_{10} = 1.0M_{\odot}$, $M_{20} = 0.9M_{\odot}$, $P = 3.0\text{d}$ and final parameters: $M_1 = 0.20M_{\odot}$, $M_2 = 1.30M_{\odot}$, $P = 1.06\text{d}$. The evolutionary tracks for the initial primary and secondary of model (1) are shown as red and dark solid lines, respectively. The corresponding tracks for model (2) are indicated as gray and light red lines. The dashed lines indicate locations of constant radius (from lower left to upper right: $1R_{\odot}$, $2R_{\odot}$, $3R_{\odot}$). The locations of four cool Algols in Table 6 are shown as open symbols. Three moments in the evolution are marked for model (1): the onset of mass transfer (filled circle), orbital period reaches minimum (filled triangle) and the end of mass transfer (filled star). For model (2), only the onset of mass transfer is labeled. The Zero Age Main Sequence from MESA is indicated by the thick purple line.

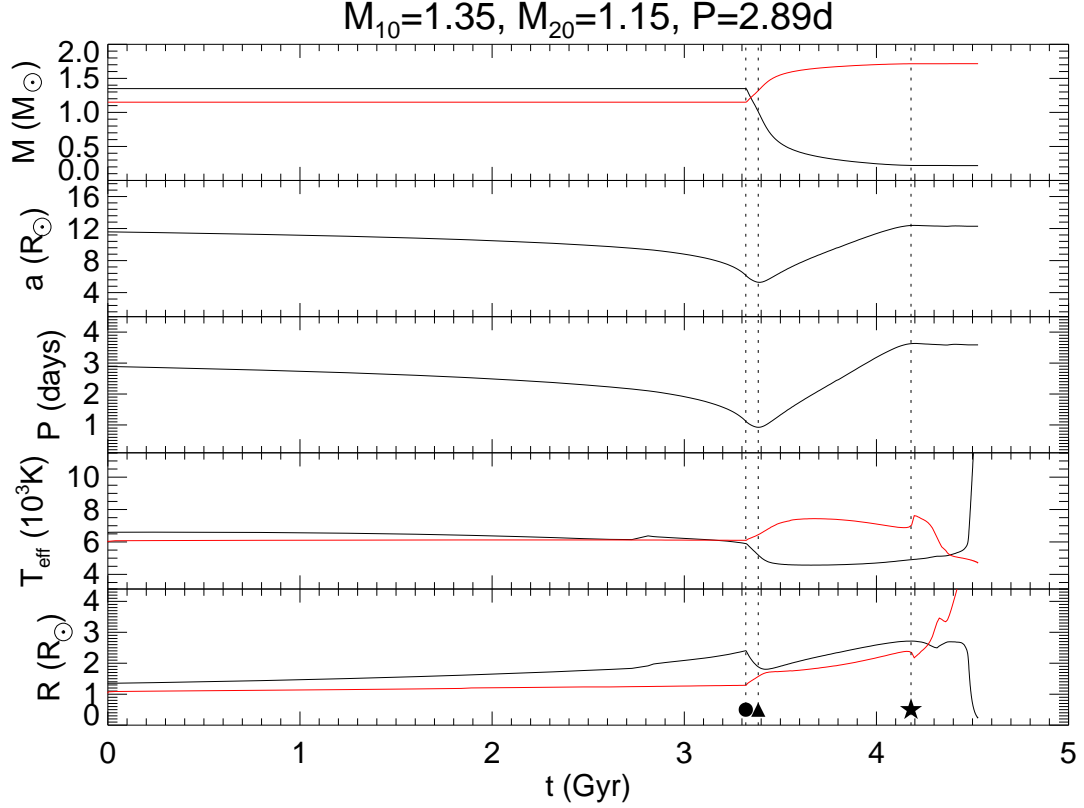


Fig. 11.— The evolution of a close binary system with initial masses $M_{10} = 1.35M_{\odot}$, $M_{20} = 1.15M_{\odot}$ and initial period $P = 2.89$ days (model (1), see text). The parameters mass (M), semi-major axis (a), period (P), effective temperature (T_{eff}), and radius (R) are shown as a function of time (t). The initially more massive star (donor) is indicated as black solid line and the mass gainer is shown in red. The vertical dashed lines label three important moments in the evolution: the onset of mass transfer (filled circle), orbital period reaches minimum and mass ratio reversal occurs (filled triangle), and the end of mass transfer (filled star). Please see text for more details.